Status of Al$_2$O$_3$/TiO$_2$-Based Antireflection and Surface Passivation for Silicon Solar Cells

Dongchul Suh

Inhibiting charge recombination effectively by surface passivation is very important for high-efficiency silicon solar cells. With the emergence of passivated emitter and rear cells (PERCs), which surpass conventional solar cells, the need for a novel passivation scheme is increasing. Passivation layer stacks using negatively charged Al$_2$O$_3$ have been applied successfully to realize high-efficiency PERC solar cells. Herein, the developments of surface passivation by Al$_2$O$_3$/TiO$_2$-based layers are reviewed. The topics range from synthesis methods and optical properties as antireflection coatings to the electrical properties related to the material, interface, and passivation quality. Ultrathin Al$_2$O$_3$/TiO$_2$-based layers generally feature a combination of field-effect passivation by negative fixed charges, a low interface defect density, and adequate humidity stability. Among the various deposition methods, atomic layer deposition is focused on, which can form dual layers and nanolaminates. How the features of atomic-layer-deposited Al$_2$O$_3$/TiO$_2$-based layers can be utilized for interface engineering and tailoring the properties of surface passivation schemes is discussed.

1. Introduction

For more than 20 years, most solar cells have been manufactured using silicon wafers with a screen-printed full-area aluminum layer on the rear surface.[1] Charge carrier recombination at the silicon and aluminum layer interface is restrained insufficiently by aluminum doping in the silicon, which forms the aluminum back-surface field (Al-BSF).[2–4] This Al-BSF partly reflects long-wavelength light, decreasing light absorption in silicon solar cells. Thus, the efficiency of most industrial silicon solar cells with Al-BSF is restricted to ≈20%.[5] Passivated emitter and rear cells (PERCs) that overcome these limitations are completely introduced to mass production by many solar cell manufacturers because of higher compatibility and efficiencies with minimized modification required on existing production lines.[6,7]

PERC solar cells add a rear passivation scheme to the standard full-area Al-BSF cell, specifically involving the deposition of a passivation film. In the first PERC solar cell proposed by Blakers et al., a silicon dioxide layer was applied to minimize the recombination of charge carriers and increase the internal reflectivity and absorption of infrared light.[8] Generally, passivation layer stacks such as Al$_2$O$_3$/SiN$_x$ or SiO$_2$/SiN$_x$ are applied as a rear-side passivation scheme for high-efficiency PERC cells.[9–15] The doping type and Si resistivity determine the suitability of a passivation scheme, with the consideration of the thermal, UV, and long-term stability, the optical properties (i.e., parasitic absorption and refractive index), and the processing requirements (e.g., surface cleaning and available synthesis methods).[16] Ultrathin Al$_2$O$_3$ films down to a few nanometers in thickness show a combination of field-effect passivation by negative fixed charges and a low interface defect density.[17–20] The use of an Al$_2$O$_3$/SiN$_x$ dual layer enhances the passivation effect because this stack exhibits a negative fixed charge density, and the top SiN$_x$ layer improves the chemical stability in protecting Al$_2$O$_3$ films from the undesired reaction caused by aluminum paste during firing.[14,21,22] Because the ultrathin transparent Al$_2$O$_3$ is insufficient for rear reflection of the solar cell, the SiN$_x$ layer with higher refractive index can also improve the long-wave response, resulting in a higher short-circuit current.[16] The extinction coefficient of a-SiN$_x$:H films increases greatly, especially below 600 nm, as the Si:N ratio increases, which is undesirable for applications as an antireflection coating.[23] Over the years, various material stacks with fixed charges were investigated for surface passivation of solar cells.[24–32] Passivation schemes using Al$_2$O$_3$/TiO$_2$ stacks with outstanding performance have been developed. This Review discusses the progress in the development and understanding of the properties of Al$_2$O$_3$/TiO$_2$-based surface passivation schemes over the last few years. A TiO$_2$ single layer has been used conventionally for antireflection coatings and the surface passivation of silicon solar cells.[33–37] TiO$_2$ has a relatively high refractive index and low extinction coefficients for wavelengths down to 400 nm.[23] Therefore, TiO$_2$ is also a good candidate as the top layer of the Al$_2$O$_3$/dielectric stack because of its excellent optical properties. A graded refractive index can be obtained using a continuous alternating Al$_2$O$_3$ and TiO$_2$ ALD process between extremes given by the refractive indices of the two materials, allowing further decreases in optical reflectance.[38]

The focus will be on pseudobinary alloys, dual layers, and nanolaminates composed of Al$_2$O$_3$ and TiO$_2$ deposited by various

D. Suh
Department of Chemical Engineering
Hoseo University
Asan 31499, Republic of Korea
E-mail: dcsuh@hoseo.edu

The ORCID identification number(s) for the author(s) of this article can be found under https://doi.org/10.1002/pssr.202100236.

methods such as atomic layer deposition and sol–gel processes used for silicon surface passivation. The development and applications of Al_2O_3/TiO_2-based passivation schemes depend on an understanding of the properties underlying the formation and major properties of the stacks.

2. Synthesis and Optical Properties for Antireflection

2.1. Sol–Gel Method

The sol–gel method uses the hydrolysis and condensation of organometallic precursors on a silicon substrate. The precursors are deposited by spin coating and then annealed to obtain thin films. This process has the advantage of easy and inexpensive operation over other methods.

A thin film of pseudobinary alloys $(Al_2O_3)_x(TiO_2)_{1-x}$ was prepared using organometallic precursors, such as an aluminum sol, $Al(C_2H_5O)_3$, from aluminum chloride, and peptized titanium sol from titanium ethoxide.[39–42] Both sols were mixed at suitable ratios, and solutions with different aluminum contents were used. The shift in the fundamental absorption edge toward shorter wavelengths was observed when x in $(Al_2O_3)_x(TiO_2)_{1-x}$ was increased, which means that the bandgap increases with increasing Al content. A close dependence of the refractive index and bandgap on Al content enables the tailoring of the optical properties of these oxide thin films by adjusting their composition.

2.2. Spray Pyrolysis

An Al_2O_3/TiO_2 double-layer antireflection coating (ARC) film formed by spray pyrolysis was introduced as a nonvacuum processing method.[43] The spray pyrolysis deposition of precursor solutions using a glass atomizer formed Al_2O_3 and TiO_2 films on the silicon wafers at a deposition temperature of 450 °C. The Al_2O_3 precursor solution was 0.03 mole L^{-1} of aluminum (III) acetylacetonate $(Al(acac)_3)$ in ethanol. The TiO_2 precursor solution was prepared by a tenfold dilution of titanium bis-isopropoxidebis-acetylacetone (TAA) (prepared by mixing titanium (VI) isopropoxide and acetylacetone at a 1:2 mole ratio) in ethanol. The film thickness of the Al_2O_3 layer and TiO_2 layer was controlled by the amount of sprayed precursor solution. Fourier transform infrared spectroscopy showed that hydrocarbon-based organics could remain inside the formed layer because of the organics contained in the precursor solution.

By applying the double-layer ARC film on the flat and textured silicon surfaces, the reflectivity was reduced considerably to a minimum of 0.2% and 0.4% at $\approx$700 and 600 nm, respectively. As a result, the average reflectance on flat and textured Si surfaces was 20.1% and 9.71%, respectively. The Al-BSF solar cells with the 90 nm Al_2O_3/40 nm TiO_2 double-layer ARC film showed that the J_{SC} of solar cells with a flat and textured surface was around 34.3 and 37.0 mA cm^{-2}, which was improved by 6.7 and 3.5 mA cm^{-2}, respectively, compared to the case without ARC.

2.3. Atomic Layer Deposition (ALD)

2.3.1. Dual Layer

The stack layers consisting of a thin Al_2O_3 layer and a TiO_2 capping layer deposited by ALD have been investigated intensively.[44–48] Of particular interest are stacks where the Al_2O_3 layer is sufficiently thin (generally of the order of 10 nm or less), so it has minimal impact on the optical properties of the stack because Al_2O_3 has a low refractive index ($\approx$1.6) that decreases the antireflection performance of the dual-layer coating. The thickness of TiO_2 is less than 50 nm for the same purpose in that a dual-layer stack of 10 nm Al_2O_3 followed by 50 nm of TiO_2 is optimal.[44]

In addition, the entire Al_2O_3/TiO_2 stack can be deposited by ALD in the same chamber with excellent layer thickness control and the efficient use of chemical precursors. Trimethylaluminum $Al(CH_3)_3$ was generally used as the aluminum precursor, and titanium chloride $TiCl_4$, tetrakis-dimethylamino-titanium $Ti(N(CH_3)_2)_4$, and titanium tetrakis-isopropoxide $Ti(OCH(CH_3)_2)_4$ were used as the titanium precursor. H_2O, O_3, and remote O_2 plasma were used as the oxidants for Al_2O_3 and TiO_2 films. The films were prepared by alternating the metal precursor and oxidant exposure. The deposition rates of Al_2O_3 and TiO_2 at 200 °C were $\approx$0.1–0.11 and 0.035–0.05 nm per ALD cycle, respectively. For surface passivation, the stack was usually annealed in N_2 or O_2 ambient at $\approx$400 °C.

The reflectivity with Al_2O_3/TiO_2 dual-layer coating was significantly reduced on flat and textured wafers coated with 10 nm Al_2O_3/50.5 nm TiO_2, where 1.8% and 1% decreases in absolute reflectivity were estimated, respectively, compared to standard silicon nitride.[44] This corresponds to an additional $\approx$0.4 mA cm^{-2} in current, or several tenths of a percentage point in efficiency.

Nanotextured black silicon solar cells composed of Si nanowire arrays and a 10 nm Al_2O_3/10 nm TiO_2 dual-layer passivation stack on the n^+ emitter were fabricated.[47] The diffused junction depth was $\approx$0.4 µm and the surface dopant concentration was $\approx$5 × 10^{20} cm^{-3}. The short-circuit current density and efficiency of the solar cell were increased by 11% and 20%, respectively, because the Al_2O_3/TiO_2 dual-layer passivation stack suppresses the total reflectance over a broad range of wavelengths (400–1000 nm).

2.3.2. Nanopatterned Coating

For ultralow surface recombination, a nanopatterned coating was presented for crystalline silicon solar cells that combines the antireflection and passivation properties.[49] The nanopatterned coating comprised an array of TiO_2 nanocylinders placed on top of a 30 nm thick Al_2O_3/50 nm thick TiO_2 dual layer on a flat silicon wafer. TiO_2 nanocylinders and layers of stacks except for Al_2O_3 were deposited by electron beam evaporation from a TiO_2 source. The TiO_2 nanocylinders had a diameter, height, and pitch of 350, 100, and 500 nm, respectively. This combined geometry yielded an average reflectivity of 2.8% weighed over the AM 1.5 solar spectrum in the 420–980 nm spectral range.

2.3.3. Nanolaminates

The refractive index of laminated coatings consisting of alternating stacks of nanoscale Al_2O_3 and TiO_2 sublayers grown by ALD can be controlled.[30,38,50–56] If the refractive index of film materials is easy to adapt for optical coatings, it enables the flexible design of multilayer optical applications. The structure appears to be optically continuous when the layer thickness is much less than the wavelength of interest. In addition, this method can be used to fabricate coatings with a refractive index varying in the thickness direction (gradient-index coatings), which have attractive spectral performance exceeding that of regularly stacked normal multilayer coatings.[57]

The desired average refractive index can be obtained by adjusting the relative thickness of the high- and low-refractive–index-layer results. The refractive indices for pure Al_2O_3 and TiO_2 are 1.61 and 2.39, respectively. The average refractive index can be varied by adjusting only the number of growth cycles of each precursor. The precursors used for forming Al_2O_3/TiO_2 nanolaminates are the same as those for the dual-layer. Zaitsu et al. deposited an Al_2O_3/TiO_2 laminated coating of which the refractive index changed linearly from 1.870 to 2.318 as the thickness of the single TiO_2 sublayer obtained from the $TiCl_4$ precursor was varied from 0.2 to 3.9 nm while that of the single Al_2O_3 sublayer was kept constant at 0.55 nm.[38] They showed a reflectance of 0.3% on flat substrates at the wavelength of 560 nm from the laminated coating consisting of 60 pairs of sublayers, with a refractive index of 1.91. The estimated thicknesses of the Al_2O_3 and TiO_2 single layers were 0.55 and 0.39 nm, respectively.

Ultrathin Al_2O_3/TiO_2 nanolaminate structures were deposited by ALD with layer thicknesses ranging from 0.1 to 50 nm and characterized by X-ray reflectivity.[51] The results showed that the individual layers within the nanolaminate remain discrete for dual layers as thin as 0.8 nm, where individual layer thickness is ≈0.4 nm. Further decreases in the dual-layer thickness produce a composite of the two materials ($Ti_xAl_yO_z$).

The spectroscopic ellipsometry method was also used to obtain optical constants of the nanolaminates.[52] The refractive index and extinction coefficient of TiO_2 decreased and blueshifted with increasing number of dual layers, which was related to the improvement of the crystalline structure and increases in the packing density.[58,59] Although a previous study reported that the refractive index of the TiO_2 nanolayer in the Al_2O_3/TiO_2 nanolaminates increased and saturated when the TiO_2 monolayer thickness exceeded 25 nm because of nucleation and film growth,[60] the saturation of refractive indices was not observed in this work resulting from different nucleation rates and the layer structures.

Particular attention was paid to the properties of the Al_2O_3/TiO_2 nanolaminate structures constructed on silicon substrates using ALD by alternatively depositing a TiO_2 sublayer and Al_2O_3 partial monolayer.[55] Each nanolaminate incorporated a certain number of Al_2O_3 partial monolayers, with this number ranging from 10–90 in Al_2O_3/TiO_2 nanolaminates grown during 2700 total reaction cycles of TiO_2 at 250 °C. The results show clearly that the changes in the fundamental properties of the Al_2O_3/TiO_2 nanolaminates have little influence on the optical properties such as the bandgap and transmittance, even though Al_2O_3 partial monolayers as an internal barrier promoted structural inhomogeneity in the film.

3. Electrical Properties for Surface Passivation

3.1. Passivation Performance

In the electrical properties of 46 nm thick pseudobinary alloys $(Al_2O_3)_x(TiO_2)_{1-x}$ films, the negative fixed charge Q_f increased to 7.5×10^{11} cm^{-2} when the annealing temperature was 750 °C.[40] The negative fixed charge at the interface with the p-type Si induces accumulation regions on the semiconductor surface. As a result, surface band bending occurs, similar to when a surface p$^+$ region is present (back-surface field effect), and a decrease in surface recombination can be expected. Surface recombination velocities (SRVs) as low as 80 and 150 cm s^{-1} have been measured on a 7 Ω cm polished float zone (FZ) wafer and 1 Ω cm Czochralski (CZ) wafer, respectively. The best result was achieved on multicrystalline silicon (300 cm s^{-1}).[40] The interface trap density D_{it} of 7×10^{11} eV^{-1} cm^{-2} was obtained in the center of the bandgap with Terman's method.

In the case of an Al_2O_3/TiO_2 dual layer deposited by spray pyrolysis, it is difficult to check passivation properties because there was little difference in the open-circuit voltage (V_{oc}) regardless of the ARC applied in this work. Furthermore, the textured solar cells with ARC had a significantly low efficiency of 15.5%.[43]

When the dual layer with 10 nm Al_2O_3/50.5 nm TiO_2 was used, the maximum surface recombination velocity was below 25 cm s^{-1} for injection levels up to 10^{16} cm^{-3} in a CZ p-type 3 Ω cm silicon wafer with a thickness of 400 μm, indicating a V_{oc} of ≈700 mV at 1 sun illumination intensity.[44]

Suh et al. applied a 10 nm Al_2O_3/50 nm TiO_2 dual layer to the passivation of a boron emitter with a sheet resistance of 100 Ω sq^{-1} for an n-type 100 Ω cm FZ silicon wafer with a thickness of 500 μm.[48] They obtained a low J_{0e} (emitter saturation current density) value of 22.7×10^{-15} A cm^{-2}, which corresponds to a maximum 1 sun V_{oc} of 711 mV if the short-circuit current density is 40 mA cm^{-2}, which conventional silicon solar cells can usually achieve. The passivation level of Al_2O_3/TiO_2 annealed at 300 °C was comparable to that of the samples annealed at 400 °C, even though the J_{0e} value decreased more slowly. The Q_f value and the D_{it} were extracted from the high-frequency capacitance–voltage characteristics of each film. Compared to the Al_2O_3 sample (2.1×10^{12} cm^{-2}), the Al_2O_3/TiO_2 sample had a significantly higher negative charge density of 9.5×10^{12} cm^{-2}. Negative charges are present not only at the Si/Al_2O_3 interface but also within the TiO_2 film or (more likely) at the Al_2O_3/TiO_2 interface.[45] This charge is sufficient for field-effect passivation because empirically, the degree of field-effect passivation is generally saturated at a charge density of ≈5×10^{12} cm^{-2}.[61] The D_{it} value of the Al_2O_3/TiO_2 stack (6.0×10^{12} eV^{-1} cm^{-2}) was slightly higher than that obtained for the Al_2O_3 single layer (3.2×10^{12} eV^{-1} cm^{-2}).[48] The improved passivation of the Al_2O_3/TiO_2 stack was attributed to the enhanced field-effect passivation despite the deteriorated chemical passivation.

A high efficiency of 18.5% and V_{oc} of 590 mV was achieved in nanotextured black silicon solar cells with an n^+ emitter passivated by a 10 nm Al_2O_3/10 nm TiO_2 dual layer in a CZ p-type 0.5–3 Ω cm silicon wafer with a thickness of 180 μm.[47] The conventionally alkaline textured silicon solar cell passivated by the same stack had an efficiency of 17.9% and a V_{oc} of 597 mV. The Al_2O_3/TiO_2 dual-layer stack treated by annealing in the forming gas achieved a high positive Q_f (4.7×10^{12} cm^{-2}) and low D_{it} (3.9×10^{11} eV^{-1} cm^{-2}). This also had the effective minority carrier lifetime of 34.25 μs and implied a 1 sun V_{oc} of 619 mV.

Crystalline silicon wafers covered with a nanopatterned 30 nm Al_2O_3/50 nm TiO_2 dual-layer coating, including TiO_2 nanocylinders fabricated by electron beam evaporation, exhibited carrier lifetimes of up to 4.1 ms for injected carrier densities of 10^{15} cm^{-3} in an n-type 2.5 Ω cm FZ silicon wafer with a thickness of 270 μm.[49] This corresponded to a maximum effective surface recombination velocity of only 3.3 cm s^{-1}.

Ultrathin 0.5 nm Al_2O_3/1.5 nm TiO_2 stacks were used to form electron-selective contacts for interdigitated back-contacted n-type c-Si solar cells. A specific contact resistance of 2.5 m Ω cm^2 was measured together with surface recombination velocities below 40 cm s^{-1} in FZ n-type c-Si wafers with a resistivity of 2 Ωcm and a thickness of 280 μm.[62] A thin 18 nm thick ZnO was inserted between the Al_2O_3/TiO_2 passivation layers and the metal contact to improve the rear reflector properties. Significant improvement in 280 μm thick n-type silicon wafers with a resistivity of 2.5 Ωcm was obtained for annealing temperature of 225–250 ℃ with SRV values as low as 14 cm s^{-1} corresponding to an implied open-circuit value of 688 mV.[63]

The dual-layer stack consisting of a 5 nm Al_2O_3 interface layer and a 15 nm TiO_2 capping layer on a p-type 1–3 Ωcm FZ silicon wafer with a thickness of 250 μm showed a surface recombination velocity of $\approx$15 cm s^{-1}.[56] With this stack, a contact resistance of 20 Ωcm^2 was also achieved. A 1.8 nm Al_2O_3/3 nm TiO_2 layer on H-terminated Si (p-type, FZ Si, 280 μm thickness, and resistivity of 2.8 Ωcm) yielded an SRV value of 20 cm s^{-1} with a corresponding contact resistance of 0.02 Ωcm^2 before postdeposition annealing.[64]

A dual-layer system consisting of a passivating Al_2O_3 deposited by ALD and a conducting TiO_x by sputtering was proposed to use a full area contact for PERC solar cells.[65] A 250 μm thick p-type FZ Si wafer with a resistivity of 2 Ωcm was used to determine the passivation behavior. The SRV of the 3 nm Al_2O_3/17 nm TiO_x deposited by ALD reached 30 cm s^{-1} for 3 nm Al_2O_3, whereas a sputtered TiO_x layer on top of the 3 nm ALD Al_2O_3 improved the SRV to $\approx$10 cm s^{-1}. In contrast, sputter damage reduced the lifetime. The 3 and 6 nm Al_2O_3 samples had a lifetime of 250 μs and 1 ms, respectively. In addition, doping of the TiO_x by Ta improved the conductivity of TiO_x, reducing the measured stack resistance at 40 mA cm^{-2} by 40 % from 20 to 12 Ωcm^2.

Figure 1 shows surface recombination velocities of silicon wafers passivated with Al_2O_3/TiO_2 dual layers. Most were evaluated with Al_2O_3 thicknesses less than 10 nm, indicating that it can give a reasonable level of passivation. On the other hand, sub 3 nm Al_2O_3 samples generally have an SRV higher than 20 cm s^{-1}, so it is desirable to utilize thicker Al_2O_3 (e.g., 5 nm or more) for dual-layer passivation. The passivation of dual layers improved as the Al_2O_3 thickness increased. Thick TiO_2 capping
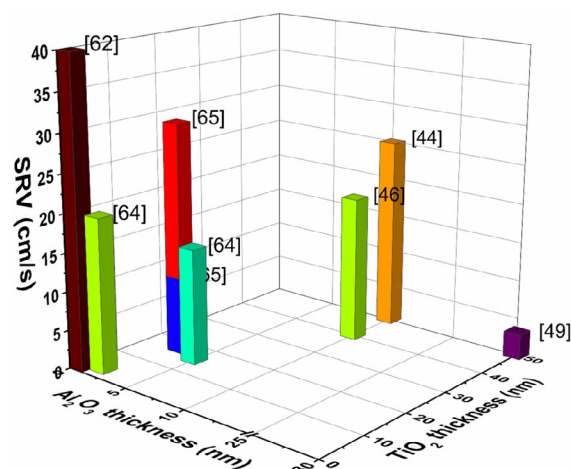

Figure 1. Surface recombination velocities of silicon wafers passivated with Al_2O_3/TiO_2 dual layers. The labels are designated as reference numbers.

layers are usually used as antireflection coatings, but thin TiO_2 capping layers have recently been preferred because of their potential to passivate contacts.[62,64–66] In particular, the sputtered TiO_x sample has a very low SRV value of 10 cm s^{-1} compared to other ALD samples.[65]

Nanolaminates are usually used with an Al_2O_3 interface layer or Al_2O_3/TiO_2 dual layer for effective surface passivation. The interaction of Al_2O_3 and TiO_2 strongly influences electrical transport during layer growth. The effective carrier lifetime of 15 nm thick nanolaminates with a 5 nm thick Al_2O_3 interface layer on p-type 250 μm thick FZ Si with a resistivity of 1–3 Ωcm was similar to that of 5 nm Al_2O_3/15 nm TiO_2 ($\approx$0.8 ms).[56] The effective carrier lifetime of these nanolaminate stacks increased gradually up to 5 ms with increasing Al_2O_3 interface layer thickness to 20 nm.

These Al_2O_3/TiO_2 nanolaminates provide an improved silicon surface passivation compared to conventional Al_2O_3 films.[30] The effective carrier lifetime measurements showed that Al_2O_3/TiO_2 nanolaminates achieved values of up to 6.0 ms in p-type FZ Si wafers with a resistivity of 2 Ωcm and a thickness of 250 μm at a TiO_2 concentration of 0.2%, corresponding to an ALD cycle ratio of Al_2O_3:$TiO_2 = 70:1$. The TiO_2 sublayer thickness was 0.016 nm, which was measured by scanning transmission electron microscopy. The total passivation layers had a thickness of $\approx$30 nm. Electrical measurements showed that TiO_2 incorporation causes strong hysteresis effects, which are linked to the trapping of negative charges and result in enhanced field-effect passivation, showing a density of negative fixed charges in the range of 2×10^{12} cm^{-2} and D_{it} values (5×10^{10} eV^{-1} cm^{-2}) below the detection limit of the applied method. In contrast, higher TiO_2 concentrations led to a continuous decrease in the effective minority carrier lifetime to values below 1.0 ms at a TiO_2 concentration of 9%. In contrast, pure Al_2O_3 passivation resulted in a carrier lifetime of 4.5 ms after the subsequent annealing in forming gas.

The performance of nanolaminates for silicon surface passivation was found for boron diffusion with a sheet resistance of 230 Ω sq^{-1} in n-type 100 Ω cm FZ silicon wafers with a thickness

of 500 μm.[53] Dual layers and nanolaminates composed of Al_2O_3/TiO_2 layers were deposited sequentially without a vacuum break on both sides of the silicon wafer in the same reaction chamber. There was a difference in the position at which the nanolaminates were placed in the samples. One was a 20 nm thick nanolaminate deposited between a 10 nm thick Al_2O_3 interlayer and the uppermost 35 nm thick TiO_2 layers (Al_2O_3/ nanolaminates/TiO_2, ANT structure). The other was that on the top of a 10 nm thick Al_2O_3/35 nm thick TiO_2 stack (Al_2O_3/TiO_2/nanolaminates, ATN structure). Al_2O_3/TiO_2 nano-laminates were prepared by the repeated deposition of 1.1 nm thick Al_2O_3 and 0.9 nm thick TiO_2. The J_{0e} values of the two structures were similar ($\approx 20 \times 10^{-15}$ A cm^{-2} at an injection level of 5×10^{15} cm^{-3}). The most notable finding is that almost no emitter degradation occurred when the ATN structure was used for passivation. The J_{0e} remained almost at the initial value even after 10 days of humidity exposure (relative humidity of $\approx 98\%$ at 80 °C). In contrast, there was almost an order of magnitude increase in the emitter saturation current when the ANT structure was used.

Low densities of fast interface states near a midgap with a value of 4.85×10^9 eV^{-1} cm^{-2} were achieved with a 40 nm nano-laminate comprising 0.8 nm Al_2O_3 and 0.7 nm TiO_2 using ozone as the coreactant.[67] This sub-nanometer laminate on highly doped Si with more than 10^{21} atoms cm^{-3} without annealing exhibited an oxide charge density of 3.72×10^{11} cm^{-2}, which was attributed to the contribution of the positive interface charges in the dielectric stack/Si system with TiN electrodes deposited by the ALD process at 450 °C.[68]

Table 1 shows the lifetimes of silicon wafers passivated with Al_2O_3/TiO_2 dual layers and nanolaminates according to each layer thickness. Most of the samples were evaluated based on FZ Si and Al_2O_3, and the TiO_2 thickness was not specifically indicated in the case of nanolaminates. Similar to the result in Figure 1, the lifetime tends to increase with increasing Al_2O_3 thickness. A thick TiO_2 also leads to a high lifetime; however, sputtered TiO_x samples showed a rather low lifetime, which can be possibly attributed to the plasma damage on the silicon wafer coated with an ultrathin 3 nm Al_2O_3 layer.[65] Considering the interlayer and total thickness, the lifetimes of the

nanolaminate are similar to those of the dual layer, or there are slightly better lifetimes.

An excellent passivation level and a low contact resistivity are required to use stacks as passivating contacts successfully. **Table 2** lists the contact resistivities of silicon wafers passivated with Al_2O_3/TiO_2 dual layers and nanolaminates. These results indicate that the contact resistivity is strongly dependent on the Al_2O_3 thickness because the ALD TiO_2 used for solar cell pas-sivation is usually conductive. The dual-layer sample with a total thickness of 2 nm has the lowest contact resistivity of 0.0025 Ω cm^2.[62] The Ta-doped TiO_x sample, which has improved conduc-tivity despite its relatively thick thickness, has a lower contact resistivity than others with similar thicknesses. Nanolaminates do not tend to have a distinctly lower contact resistivity compared to the dual layer.

3.2. Effect of Annealing on Surface Passivation

Depositing pseudobinary alloys $(Al_2O_3)_x(TiO_2)_{1-x}$ films was achieved by spin coating and two subsequent annealing steps were then carried out.[41] A first annealing step was done at low temperatures (200–350 °C) to remove the organics by evapo-ration. At this stage, no negative charge was present and no nota-ble passivation was measured. After a high-temperature annealing step (650–1000 °C), molecular rearrangement took place, and a negative charge density as high as 10^{12} cm^{-2} was produced. The negative fixed charge of pseudobinary alloys films increased when the temperature rose.[69] A temperature of 750 °C was proven to be optimum for a negative fixed charge.[40] The annealing ambient had no influence at that temperature. Oxygen diffusion and silicon surface oxidation occurred at tem-peratures higher than 850 °C.

The Al_2O_3/TiO_2 dual layer deposited by ALD underwent two discrete annealing steps.[45,46] The Al_2O_3 layer was deposited first, followed by forming gas annealing at 400 °C, and the TiO_2 layer was then deposited and annealed in O_2 at 300–400 °C. Post-TiO_2 deposition, annealing was conducted in an O_2 ambient to minimize the concentration of oxygen vacan-cies and obtain stoichiometric films.[70] The J_{0e} measured imme-diately after TiO_2 deposition on annealed Al_2O_3 samples decreased considerably, particularly for an Al_2O_3 thickness below 10 nm. With the deposition of 40 nm thick TiO_2 onto the 10 nm

Table 1. Effective lifetimes of silicon wafers passivated with Al_2O_3/TiO_2 dual layers and nanolaminates.

Type	Al_2O_3 thickness [nm]	TiO_2 thickness [nm]	Total thickness [nm]	Lifetime [μs]	Ref.
Dual layer	10	10	20	34.25[a]	[47]
Dual layer	30	50[b]	80	4100	[49]
Dual layer	3	17[c]	20	250	[65]
Dual layer	6	14	20	1000	[65]
Nanolaminate	–	–	25[d]	800	[56]
Nanolaminate	–	–	40[e]	5000	[56]
Nanolaminate	–	–	30	6000	[30]

[a]Positive charge, p-type CZ Si; [b]e-beam evaporated; [c]Sputtered; [d]5 nm Al_2O_3 interlayer added; [e]20 nm Al_2O_3 interlayer added.

Table 2. Contact resistivities of silicon wafers passivated with Al_2O_3/TiO_2 dual layers and nanolaminates.

Type	Al_2O_3 thickness [nm]	TiO_2 thickness [nm]	Total thickness [nm]	Contact resistivity [Ω cm^2]	Ref.
Dual layer	0.5	1.5	2	0.0025	[62]
Dual layer	5	15	20	20	[64]
Dual layer	1.8	3	4.8	0.02	[65]
Dual layer	3	17[a]	20	20	[65]
Dual layer	6	14[b]	20	12	[65]
Nanolaminate	–	–	25[c]	20	[56]

[a]Sputtered; [b]Sputtered and Ta-doped; [c]5 nm Al_2O_3 interlayer added.

thick annealed Al_2O_3 layer, the J_{0e} value was 11×10^{-15} A cm^{-2} in the n-type 0.5–3 Ωcm FZ wafer with a thickness of 500 μm and a 230 Ω sq^{-1} boron emitter. Effective surface recombination velocity values below 22 and 19 cm s^{-1} were obtained on 0.5 Ωcm p-type and 1 Ωcm n-type FZ wafers, respectively.[46] Post-TiO$_2$ deposition annealing degraded the passivation[45,64]; the degradation after 400 °C annealing was more significant than that after 300 °C annealing, and resulted in J_{0e} values approaching those of the samples before TiO$_2$ deposition.[45] The 10 nm thick Al_2O_3/ 30 nm thick TiO_2 stack layers without post-TiO$_2$ deposition annealing showed a higher density of effective fixed charge of 4.5×10^{12} cm^{-2} than the 10 nm thick annealed Al_2O_3 single layer (2.3×10^{12} cm^{-2}). After two discrete annealing steps, the Al_2O_3/ TiO_2 stack layers had increasing effective fixed charges for higher post-TiO$_2$ deposition annealing temperatures, which reached 4.5×10^{12} cm^{-2} after 400 °C annealing. With a value of 1.1×10^{10} eV^{-1} cm^{-2} at the midgap, the D_{it} of the as-deposited TiO$_2$ on annealed Al_2O_3 was very low, and one order of magnitude lower than that of the only Al_2O_3-passivated sample. In contrast, as the post-TiO$_2$ annealing temperature increased, D_{it} increased again and reached a value of 1.1×10^{11} eV^{-1} cm^{-2} at the midgap after 400 °C annealing, which was similar to that of the only Al_2O_3-passivated sample.

Most Al_2O_3/TiO_2-based layers in this work were based on the negative charge for p-type surface passivation because both Al_2O_3 and TiO$_2$ layers typically have negative polarities.[37,71–74] In contrast, the 10 nm thick Al_2O_3/10 nm thick TiO$_2$ dual layer treated by forming gas (FG) annealing at 400 °C provided a high positive charge density,[47] which is consistent with the results reported elsewhere.[33,35] A TiO$_2$ layer with a highly positive oxide charge was deposited on the negatively charged Al_2O_3 passivation layer, resulting in a positive oxide charge in the Al_2O_3/TiO_2 dual-layer passivation stack. The D_{it} of the single TiO$_2$ layer was much higher than that of Al_2O_3 when annealed in FG, but the Al_2O_3/TiO_2 dual layer achieved surface passivation with a low D_{it}, which was provided by the bottom Al_2O_3 layer. In addition, the effects of the heat treatment sequence on passivation were investigated before and after the TiO$_2$ deposition, and a similar highly positive oxide charge ($\approx 4 \times 10^{12}$ cm^{-2}) was achieved in both cases. Slightly decreased D_{it} values of the sample annealed after TiO$_2$ deposition (3.91×10^{11} eV^{-1} cm^{-2}) were observed compared to that annealed prior to TiO$_2$ deposition (5.33×10^{11} eV^{-1} cm^{-2}). This was attributed to the interfacial states being passivated by the hydrogen in the FG and the TiO$_2$ capping layer, which is considered as a diffusion barrier, restraining the effusion of hydrogen from the Al_2O_3 layer into the air during heat treatment.[75–78] The cell performance of the sample annealed after TiO$_2$ deposition was slightly superior to that of the one annealed before TiO$_2$ deposition because of the increase of the short current density by ≈ 1 mA cm^{-2}. The SRV increased when the 1.8 nm Al_2O_3/3 nm TiO$_2$ on H-terminated Si samples was annealed in nitrogen at 300–400 °C.[64] Notable exceptions are samples with 9 nm thick Al_2O_3 layers, which then showed the lowest SRV values of 20 cm s^{-1} after 400 °C post-deposition anneal (PDA). In the case of 0.5 nm Al_2O_3/1.5 nm TiO$_2$/18 nm ZnO stacks, a significant improvement of passivation was obtained even for the lowest temperature of 150 °C and very low SRV values were maintained for 225–250 °C.[63]

The effects of the annealing temperature were analyzed by damp heat test on the passivation of nanolaminates combined with dual layer, which are Al_2O_3/nanolaminates/TiO$_2$ and Al_2O_3/TiO$_2$/nanolaminates.[53] In both passivation structures, annealing structures at a lower temperature (300 °C) yielded better passivation than at a higher temperature (400 °C). The transition of stacked TiO$_2$ from amorphous to polycrystalline phase on amorphous Al_2O_3 occurred at 400 °C annealing. This result is consistent with the X-ray diffraction measurements showing that the as-deposited TiO$_2$ layers on annealed Al_2O_3 were amorphous, and became polycrystalline (anatase phase) after post-TiO$_2$ deposition annealing at 400 °C.[45] Such a transition from amorphous to crystalline phases depends on both the annealing temperature and layer thickness. In anatase TiO$_2$, grain boundaries can serve as paths for the diffusion of moisture. Annealing at 300 °C to stacked amorphous TiO$_2$ retarded humidity penetration and was more beneficial for encapsulation. This temperature effect was much less pronounced for the Al_2O_3/TiO$_2$/nanolaminate structure than for the Al_2O_3/nanolaminates/TiO$_2$ structure. This indicates that Al_2O_3/TiO$_2$/nanolaminate structures can act efficiently as an encapsulation layer resistant to moisture penetration despite the stacked TiO$_2$ being polycrystalline.

The influence of different annealing atmospheres was examined on the carrier lifetime data for Al_2O_3/TiO$_2$ nanolaminate stacks with a 5 nm Al_2O_3 interface layer thickness.[56] A significant increase in minority carrier lifetime was found after annealing in an oxidizing atmosphere (≈ 3 ms). In contrast, the lifetime remained similar to the as-grown state after annealing in reducing (N$_2$, forming gas) atmospheres (≈ 1 ms). Annealing in O$_2$ would have improved the passivation performance of nanolaminates, which shows the same trend as in the Al_2O_3/TiO$_2$ dual layer. On the other hand, the postdeposition annealing condition also influences the conductivity of dielectric films. Particularly, the conductivity of TiO$_2$ increased after annealing in O$_2$ ambient,[56] so optimization is necessary to achieve high performance of solar cells.

Figure 2 shows the fixed charge density Q_f and interface defect density D_{it} for Al_2O_3/TiO$_2$-based layers. For successful solar cell

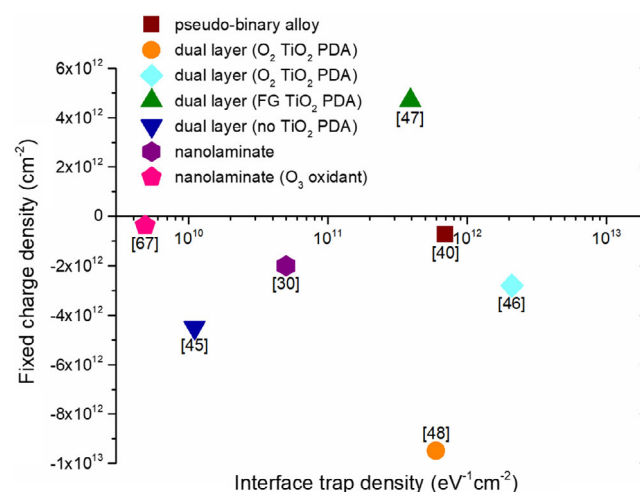**Figure 2.** Fixed charge density Q_f and interface defect density D_{it} for Al_2O_3/TiO$_2$-based layers.

passivation, both chemical passivation (D_{it}) and field-effect passivation (Q_f) must be satisfied. The pseudobinary alloy sample had a lower Q_f than the ALD samples, and the nanolaminates generally had lower D_{it} values than the dual-layer sample. A low D_{it} value could be obtained in dual-layer passivation without TiO_2 PDA, whereas TiO_2 PDA in O_2 ambient is required for a high Q_f.

4. Conclusion

Research related to Al_2O_3/TiO_2-based layers for their application to the passivation of Si surfaces has been reviewed. Several deposition methods such as the sol–gel method, spray pyrolysis, and atomic layer deposition have been used to deposit Al_2O_3/TiO_2-based layers. ALD is highly suitable for exploiting the surface and interfaces, and for modifying the properties of surface passivation schemes. Due to accurate thickness control, various structures, including dual layers and nanolaminates, can be produced. Compared to the current passivation technologies, an outstanding characteristic of the Al_2O_3/TiO_2-based layers is the field-effect passivation induced by negative fixed charges from TiO_2 and Al_2O_3. Very low defect densities $(1.1 \times 10^{11} \, eV^{-1} \, cm^{-2})$ induced by the dual layer with as-deposited TiO_2 films were obtained, which is essential for reduced surface recombination. In addition, the Al_2O_3/TiO_2 dual layer could contribute to sufficiently low emitter saturation current densities of $11 \times 10^{-15} \, A \, cm^{-2}$. In addition, annealing makes a critical impact on the passivation, depending on an ambient gas, temperature, and sequence. Annealing in an oxidizing atmosphere is beneficial to a high negative charge density, leading to enhanced field-effect passivation. For the successful implementation of Al_2O_3/TiO_2-based layers with excellent passivation properties in photovoltaic fields, it is important to obtain high-efficiency industrial solar cells and address the compatibility with mass production.

Conflict of Interest

The author declares no conflict of interest.

[1] International Technology Roadmap for Photovoltaic (ITRPV), 11th ed., **2020**, https://itrpv.vdma.org/viewer/-/v2article/render/48393879 (accessed: February 2021).

[2] V. Meemongkolkiat, K. Nakayashiki, D. S. Kim, R. Kopecek, A. Rohatgi, J. Electrochem. Soc. **2006**, 153, G53.

[3] S. Narasinha, A. Rohatgi, Conf. Record Twenty Sixth IEEE Photovoltaic Specialists Conf. - 1997, IEEE, Piscataway, NJ, USA **1997**, pp. 63–66; https://doi.org/10.1109/PVSC.1997.653925.

[4] A. Ristow, M. M. Hilali, A. Ebong, A. Rohatgi, presented at The 17th European Photovoltaic Solar Energy Conf., Munich, Germany, October 2001; available at http://hdl.handle.net/1853/26164.

[5] A. Metz, M. Fischer, J. Trube, in Proc. of the PV Manufacturing in Europe Conf., Brussels, Belgium **2017**, pp. 18–19.

[6] N. L. Chang, A. Ho-Baillie, S. Wenham, M. Woodhouse, R. Evans, B. Tjahjono, F. Qi, C. M. Chong, R. J. Egan, Sustain. Energy Fuels **2018**, 2, 1007.

[7] C. Modanese, H. Laine, T. Pasanen, H. Savin, J. Pearce, Energies **2018**, 11, 2337.

[8] A. W. Blakers, A. Wang, A. M. Milne, J. Zhao, M. A. Green, Appl. Phys. Lett. **1989**, 55, 1363.

[9] T. Dullweber, M. Siebert, B. Veith, C. Kranz, J. Schmidt, R. Brendel, B. Roos, T. Dippell, A. Schwabedissen, S. Peters, in Proc. of the 27th European Photovoltaic Solar Energy Conf., WIP, Munich, Germany **2012**, pp. 672–675; https://doi.org/10.4229/27thEUPVSEC2012-2BO.7.4.

[10] M. Hofmann, S. Janz, C. Schmidt, S. Kambor, D. Suwito, N. Kohn, J. Rentsch, R. Preu, S. W. Glunz, Sol. Energy Mater. Sol. Cells **2009**, 93, 1074.

[11] S. Gatz, H. Hannebauer, R. Hesse, F. Werner, A. Schmidt, T. Dullweber, J. Schmidt, K. Bothe, R. Brendel, Phys. Status Solidi RRL **2011**, 5, 147.

[12] P. Saint-Cast, J. Benick, D. Kania, L. Weiss, M. Hofmann, J. Rentsch, R. Preu, S. W. Glunz, IEEE Electron Device Lett. **2010**, 31, 695.

[13] G. Dingemans, M. Mandoc, S. Bordihn, M. Van De Sanden, W. Kessels, Appl. Phys. Lett. **2011**, 98, 222102.

[14] S. Mack, A. Wolf, C. Brosinsky, S. Schmeisser, A. Kimmerle, P. Saint-Cast, M. Hofmann, D. Biro, IEEE J. Photovolt. **2011**, 1, 135.

[15] S. Duttagupta, F.-J. Ma, B. Hoex, A. G. Aberle, Sol. Energy Mater. Sol. Cells **2014**, 120, 204.

[16] G. Dingemans, E. Kessels, J. Vac. Sci. Technol., A **2012**, 30, 040802.

[17] B. Hoex, J. J. H. Gielis, M. C. M. Van de Sanden, W. M. M. Kessels, J. Appl. Phys. **2008**, 104, 113703.

[18] B. Hoex, S. B. S. Heil, E. Langereis, M. C. M. van de Sanden, W. M. M. Kessels, Appl. Phys. Lett. **2006**, 89, 042112.

[19] B. Hoex, J. Schmidt, R. Bock, P. Altermatt, M. C. M. Van de Sanden, W. M. M. Kessels, Appl. Phys. Lett. **2007**, 91, 112107.

[20] J. Benick, B. Hoex, M. Van de Sanden, W. Kessels, O. Schultz, S. W. Glunz, Appl. Phys. Lett. **2008**, 92, 253504.

[21] A. Richter, J. Benick, M. Hermle, S. W. Glunz, Phys. Status Solidi RRL **2011**, 5, 202.

[22] J. Schmidt, B. Veith, R. Brendel, Phys. Status Solidi RRL **2009**, 3, 287.

[23] H. Nagel, A. G. Aberle, R. Hezel, Prog. Photovoltaics **1999**, 7, 245.

[24] G. Dingemans, N. M. Terlinden, M. A. Verheijen, M. C. M. van de Sanden, W. M. M. Kessels, J. Appl. Phys. **2011**, 110, 093715.

[25] G. Dingemans, W. Beyer, M. C. M. Van de Sanden, W. M. M. Kessels, Appl. Phys. Lett. **2010**, 97, 152106.

[26] D. Garcia-Alonso, S. Smit, S. Bordihn, W. Kessels, Semicond. Sci. Technol. **2013**, 28, 082002.

[27] G. López, P. R. Ortega, C. Voz, I. Martín, M. Colina, A. B. Morales, A. Orpella, R. Alcubilla, Beilstein J. Nanotechnol. **2013**, 4, 726.

[28] S. Y. Herasimenka, C. J. Tracy, V. Sharma, N. Vulic, W. J. Dauksher, S. G. Bowden, Appl. Phys. Lett. **2013**, 103, 183903.

[29] Y. Wan, J. Bullock, A. Cuevas, Appl. Phys. Lett. **2015**, 106, 201601.

ADVANCED
SCIENCE NEWS

www.advancedsciencenews.com

pss rrl
physica status solidi

www.pss-rapid.com

[30] F. Benner, P. M. Jordan, C. Richter, D. K. Simon, I. Dirnstorfer, M. Knaut, J. W. Bartha, T. Mikolajick, *J. Vac. Sci. Technol. B* **2014**, *32*, 03D110.

[31] B. van de Loo, H. Knoops, G. Dingemans, G. Janssen, M. Lamers, I. Romijn, A. Weeber, W. Kessels, *Sol. Energy Mater. Sol. Cells* **2015**, *143*, 450.

[32] J. Wang, S. S. Mottaghian, M. F. Baroughi, *IEEE Trans. Electron Dev.* **2012**, *59*, 342.

[33] L. Doeswijk, H. De Moor, D. H. Blank, H. Rogalla, *Appl. Phys. A* **1999**, *69*, S409.

[34] B. Richards, J. Cotter, C. Honsberg, *Appl. Phys. Lett.* **2002**, *80*, 1123.

[35] B. Richards, *Prog. Photovoltaics* **2004**, *12*, 253.

[36] B. Richards, S. Rowlands, C. Honsberg, J. Cotter, *Prog. Photovoltaics* **2003**, *11*, 27.

[37] J. Barbé, A. F. Thomson, E. C. Wang, K. McIntosh, K. Catchpole, *Prog. Photovolt: Res. Appl.* **2012**, *20*, 143.

[38] S.-i. Zaitsu, T. Jitsuno, M. Nakatsuka, T. Yamanaka, S. Motokoshi, *Appl. Phys. Lett.* **2002**, *80*, 2442.

[39] P. Vitanov, G. Agostinelli, A. Harizanova, T. Ivanova, M. Vukadinovic, N. Le Quang, G. Beaucarne, *Sol. Energy Mater. Sol. Cells* **2006**, *90*, 2489.

[40] P. Vitanov, A. Harizanova, T. Ivanova, Z. Alexieva, G. Agostinelli, *Jpn. J. Appl. Phys.* **2006**, *45*, 5894.

[41] E. Vermarien, G. Agostinelli, G. Beaucarne, J. Poortmans, in *2006 IEEE 4th World Conf. on Photovoltaic Energy Conf.*, IEEE, Piscataway, NJ, USA **2006**, pp. 103–106; https://doi.org/10.1109/WCPEC.2006.279374.

[42] P. Vitanov, T. Babeva, Z. Alexieva, A. Harizanova, Z. Nenova, *Vacuum* **2004**, *76*, 219.

[43] H. Kanda, A. Uzum, N. Harano, S. Yoshinaga, Y. Ishikawa, Y. Uraoka, H. Fukui, T. Harada, S. Ito, *Energy Sci. Eng.* **2016**, *4*, 269.

[44] B. G. Lee, J. Skarp, V. Malinen, S. Li, S. Choi, H. M. Branz, in *2012 38th IEEE Photovoltaic Specialists Conf.*, 2012, IEEE, Piscataway, NJ, USA **2012**, pp. 001066–001068; https://doi.org/10.1109/PVSC.2012.6317787.

[45] D. Suh, D.-Y. Choi, K. J. Weber, *J. Appl. Phys.* **2013**, *114*, 154107.

[46] D. Suh, K. J. Weber, *Phys. Status Solidi RRL* **2014**, *8*, 40.

[47] W.-C. Wang, M.-C. Tsai, J. Yang, C. Hsu, M.-J. Chen, *ACS Appl. Mater. Interfaces* **2015**, *7*, 10228.

[48] D. Suh, Y. Kang, *J. Nanosci. Nanotechnol.* **2017**, *17*, 5003.

[49] P. Spinelli, B. Macco, M. Verschuuren, W. Kessels, A. Polman, *Appl. Phys. Lett.* **2013**, *102*, 233902.

[50] A. Szeghalmi, M. Helgert, R. Brunner, F. Heyroth, U. Gösele, M. Knez, *Appl. Opt.* **2009**, *48*, 1727.

[51] S. Sintonen, S. Ali, O. M. Ylivaara, R. L. Puurunen, H. Lipsanen, *J. Vac. Sci. Technol. A* **2014**, *32*, 01A111.

[52] I. Iatsunskyi, E. Coy, R. Viter, G. Nowaczyk, M. Jancelewicz, I. Baleviciute, K. Załęski, S. Jurga, *J. Phys. Chem. C* **2015**, *119*, 20591.

[53] D. Suh, *Phys. Status Solidi RRL* **2015**, *9*, 344.

[54] A. Kahouli, O. Lebedev, V. H. Dao, M. B. Elbahri, W. Prellier, U. Lüders, *Appl. Phys. Lett.* **2016**, *109*, 202901.

[55] G. Testoni, W. Chiappim, R. Pessoa, M. Fraga, W. Miyakawa, K. Sakane, N. Galvão, L. Vieira, H. Maciel, *J. Phys. D: Appl. Phys.* **2016**, *49*, 375301.

[56] I. Dirnstorfer, T. Chohan, P. M. Jordan, M. Knaut, D. K. Simon, J. W. Bartha, T. Mikolajick, *IEEE J. Photovolt.* **2016**, *6*, 86.

[57] W. H. Southwell, *Opt. Lett.* **1983**, *8*, 584.

[58] I. Iatsunskyi, M. Pavlenko, R. Viter, M. Jancelewicz, G. Nowaczyk, I. Baleviciute, K. Załęski, S. Jurga, A. Ramanavicius, V. Smyntyna, *J. Phys. Chem. C* **2015**, *119*, 7164.

[59] X. Wang, G. Wu, B. Zhou, J. Shen, *Materials* **2013**, *6*, 2819.

[60] G. Triani, J. Campbell, P. Evans, J. Davis, B. Latella, R. Burford, *Thin Solid Films* **2010**, *518*, 3182.

[61] K. Weber, H. Jin, C. Zhang, N. Nursam, W. Jellett, K. McIntosh, in *Proc. of the 24th European Photovoltaic Solar Energy Conference*, WIP, Munich, Germany **2009**, pp. 534–537; https://doi.org/10.4229/24thEUPVSEC2009-1CV.4.37.

[62] G. Masmitjà, P. Ortega, J. Puigdollers, L. Gerling, I. Martín, C. Voz, R. Alcubilla, *J. Mater. Chem. A* **2018**, *6*, 3977.

[63] L. Zafoschnig, O. Villasclaras, P. Rafael, I. M. García, G. M. Rusiñol, G. L. Rodríguez, R. A. González, in *Proc. of the 35th European Photovoltaic Solar Energy Conf.*, WIP, Munich, Germany **2018**, pp. 653–656; https://doi.org/10.4229/35thEUPVSEC20182018-2AV.3.14.

[64] B. E. Davis, N. C. Strandwitz, in *2020 47th IEEE Photovoltaic Specialists Conf. (PVSC)*, IEEE, Piscataway, NJ, USA **2020**, pp. 1557–1561; https://doi.org/10.1109/PVSC45281.2020.9300502.

[65] D. Tröger, M. Grube, M. Knaut, J. Reif, J. W. Bartha, T. Mikolajick, in *Proc. of the 35th European Photovoltaic Solar Energy Conf.*, WIP, Munich, Germany **2018**, pp. 426–430; https://doi.org/10.4229/35thEUPVSEC20182018-2CO.11.3.

[66] X. Yang, Q. Bi, H. Ali, K. Davis, W. V. Schoenfeld, K. Weber, *Adv. Mater.* **2016**, *28*, 5891.

[67] A. Kahouli, M. B. Elbahri, O. Lebedev, U. Lüders, *J. Phys. Condens. Matter* **2017**, *29*, 275301.

[68] A. Kahouli, O. Lebedev, M. Ben Elbahri, B. Mercey, W. Prellier, S. Riedel, M. Czernohorsky, F. Lallemand, C. Bunel, U. Lüders, *ACS Appl. Mater. Interfaces* **2015**, *7*, 25679.

[69] P. Vitanov, A. Harizanova, T. Ivanova, K. Ivanova, *J. Mater. Sci. Mater. Electron.* **2003**, *14*, 757.

[70] Y. Takahashi, A. Ogiso, R. Tomoda, K. Sugiyama, H. Minoura, M. Tsuiki, *J. Chem. Soc., Faraday Trans. 1* **1982**, *78*, 2563.

[71] S. Lakshmi, R. Renganathan, S. Fujita, *J. Photochem. Photobiol., A* **1995**, *88*, 163.

[72] S. A. Campbell, H.-S. Kim, D. C. Gilmer, B. He, T. Ma, W. L. Gladfelter, *IBM J. Res. Dev.* **1999**, *43*, 383.

[73] A. F. Thomson, K. R. McIntosh, *Prog. Photovoltaics* **2012**, *20*, 343.

[74] M. Vasilopoulou, D. G. Georgiadou, A. Soultati, N. Boukos, S. Gardelis, L. C. Palilis, M. Fakis, G. Skoulatakis, S. Kennou, M. Botzakaki, *Adv. Energy Mater.* **2014**, *4*, 1400214.

[75] N. Balaji, C. Park, S. Lee, Y.-J. Lee, J. Yi, *J. Nanosci. Nanotechnol.* **2016**, *16*, 10659.

[76] B. Vermang, H. Goverde, A. Lorenz, A. Uruena, G. Vereecke, J. Meersschaut, E. Cornagliotti, A. Rothschild, J. John, J. Poortmans, in *2011 37th IEEE Photovoltaic Specialists Conf.*, IEEE, Piscataway, NJ, USA **2011**, pp. 003562–003567; https://doi.org/10.1109/PVSC.2011.6185916.

[77] P. Saint-Cast, D. Kania, R. Heller, S. Kuehnhold, M. Hofmann, J. Rentsch, R. Preu, *Appl. Surf. Sci.* **2012**, *258*, 8371.

[78] G. Dingemans, M. C. M. van de Sanden, W. M. M. Kessels, *Phys. Status Solidi RRL* **2011**, *5*, 22.

ADVANCED
SCIENCE NEWS

www.advancedsciencenews.com

pss rrl
physica status solidi

www.pss-rapid.com

Dongchul Suh is an associate professor of chemical engineering at Hoseo University. He was a research professor of the Global Frontier Center for Multiscale Energy Systems at Seoul National University in South Korea. He was involved in the fabrication of perovskite/silicon tandem solar cells. Before joining GFC-MES, he was a research fellow at the Centre for Sustainable Energy Systems (CSES) at The Australian National University. He established an ALD process made of various metal oxide precursors for silicon solar cell passivation. Previously, he was a senior engineer of the Development Group of Solar Energy Business Team in Samsung Electronics for 7 years.